

Few-Shot Left Atrial Wall Segmentation in 3D LGE MRI via Meta-Learning

Yusri Al-Sanaani¹, Rebecca Thornhill^{1,2}, Pablo Nery³, Elena Peña², Robert deKemp^{1,3}, Calum Redpath³, David Birnie³, Sreeraman Rajan¹

¹Department of Systems and Computer Engineering, Carleton University, Ottawa, Canada

²Department of Radiology, Radiation Oncology, and Medical Physics, University of Ottawa, Ottawa, Canada,

³Division of Cardiology, Department of Medicine, University of Ottawa Heart Institute, Ottawa, Canada.

yusrialsanaani@cmail.carleton.ca

Abstract—Segmenting the left atrial wall from late gadolinium enhancement magnetic resonance images (MRI) is challenging due to the wall’s thin geometry, low contrast, and the scarcity of expert annotations. We propose a Model-Agnostic Meta-Learning (MAML) framework for K-shot (K = 5, 10, 20) 3D left atrial wall segmentation that is meta-trained on the wall task together with auxiliary left atrial and right atrial cavity tasks and uses a boundary aware composite loss to emphasize thin structure accuracy. We evaluated MAML segmentation performance on a hold-out test set and assessed robustness under an unseen synthetic shift, and on a distinct, local cohort. On the hold-out test set, MAML appeared to improve segmentation performance compared to the supervised fine-tuning model, achieving a Dice score (DSC) of 0.64 vs. 0.52 and HD95 of 5.70 vs. 7.60 mm at 5-shot, and approached the fully supervised reference at 20-shot (0.69 vs. 0.71 DSC). Under unseen shift, performance degraded but remained robust: at 5-shot, MAML attained 0.59 DSC / 5.99 mm HD95 on the unseen domain shift and 0.57 DSC / 6.01 mm HD95 on the local cohort with consistent gains as K increased. These results suggest that more accurate and reliable thin wall boundaries are achievable in low shot adaptation, and potentially enabling clinical translation with minimal additional labeling needed for the assessment of atrial remodeling.

Keywords—Left atrium, atrial wall segmentation, LGE MRI, few-shot learning, meta-learning, MAML, domain shift

I. INTRODUCTION

Segmenting the left atrium (LA) wall in late gadolinium enhancement (LGE) MRI scans has shown promise for the characterization of atrial remodeling and for guiding ablation in patients with atrial fibrillation [1], [2]. However, accurate LA wall segmentation remains very challenging because the wall is thin, has low contrast relative to adjacent tissues, and exhibits partial-volume effects that amplify annotation variability and model uncertainty [3]–[6]. Furthermore, manual delineation is labor-intensive and sensitive to variations in scan quality, making high-fidelity LA wall labeling impractical for large-scale use across institutions [6]. While deep learning has advanced cavity segmentation [7] and joint cavity-scar frameworks [8], [9], automating the extraction of the thin atrial wall remains the weakest link in the pipeline. In particular, recent multi-centre benchmarks report left atrial cavity Dice (DSC) scores >0.90 with surface errors <1 mm, whereas the state-of-the-art LA wall segmentation models typically achieve DSC scores between 0.66–0.72 with larger surface-distance errors, underscoring that the ultra-thin atrial shell remains the principal issue to resolve [10]–[12]. Reviews of the literature in this area highlight three issues: thinness and class imbalance, open pulmonary vein/mitral valve (PV/MV) boundaries, and domain variability across centers [5]. Even the state-of-the-art methods require dozens of labeled volumes to approach human-level performance [6]. Public, labeled LGE datasets

are scarce and costly to acquire, and expert annotation of 3D atrial structures is labor-intensive [2]. Therefore, there is strong motivation to develop segmentation techniques that can achieve high accuracy with very few annotated examples.

Few-shot learning has emerged as a promising paradigm to address label scarcity in medical image analysis [13], [14]. By leveraging prior knowledge from related tasks, a model can rapidly adapt to new target structures or imaging domains using only a small number (K) of training samples. In segmentation, common few-shot approaches include metric-learning methods that compute prototype representations for foreground/background from support examples [15], and optimization-based meta-learning methods that learn to fine-tune efficiently on new tasks [13], [14]. For example, Tang et al. (2025) developed a prototype refinement network that improved few-shot organ segmentation by clustering and refining feature embeddings [15]. Model-Agnostic Meta-Learning (MAML) is a gradient-based meta-learning algorithm (optimization-based) that has shown effective fast adaptation in various domains [16]. MAML learns an initialization of model parameters such that only a few gradient steps on a new task yield good performance. MAML has been applied to medical image segmentation problems to improve data efficiency. For example, Alsaleh et al. [13] employed MAML with a 3D U-Net to demonstrate substantial gains in 5-shot settings; however, their work focused on large, distinct organs (e.g., liver and spleen) in CT scans. Khadka et al. (2022) proposed an implicit MAML algorithm for few-shot segmentation and showed 2–4% Dice gains over standard MAML on polyps and skin lesions segmentation [14]. Gama et al. (2021) applied MAML to 2D chest X-ray segmentation with simulated sparse labels, using a “mini U-Net” to mitigate memory costs [17]. They found meta-learned initialization enabled dense prediction from sparse annotations. For LGE LA segmentation, recent work has investigated few-shot approaches by learning adaptive inference mechanisms to cope with low-contrast scenarios for LA cavity segmentation [18]. Prototype methods [15] rely on the assumption that the support and query features cluster tightly in a fixed embedding space. Conversely, MAML assumes that the embedding space itself must adapt. For a structure like the LA wall, which suffers from severe partial volume effects that blur feature clusters, an optimization-based adaptation like MAML should theoretically offer superior boundary refinement capabilities compared to prototype averaging.

Another key problem is robustness to domain shift in LGE MRI, which is ubiquitous in medical imaging due to differences in scanner vendor, acquisition protocol, reconstruction pipeline, image resolution, intensity non-uniformity, noise, and site-specific preprocessing, any of which can degrade segmentation performance when models are applied outside of the training domain [6], [19], [20]. Domain generalization remains challenging in medical

imaging, as models often overfit to acquisition-specific characteristics [14]. An emerging benefit of meta-learning is improved generalization across domains, as training on a distribution of tasks encourages representations that are less specific to a single data source. Some recent studies incorporate domain shifts as different tasks during meta-training. For segmentation, this can involve meta-training on images with different simulated corruptions or from different datasets, and is related to techniques such as data augmentation, style transfer, and domain-adaptive normalization that have been proposed to improve cross-domain robustness [19], [21].

Prior few-shot LA segmentation studies focus on larger structures, such as the LA cavity [18] or large organs in CT [13], rather than the ultra-thin atrial wall; moreover, robustness to domain variability is seldom evaluated in those works. To our knowledge, meta-learning has not been applied to LGE atrial wall segmentation before. We address this gap by targeting the LA wall (myocardium) as a test case for few-shot meta-learning. We also integrate controlled domain differences into the meta-learning process, defining tasks that vary not only in target structure but also in image domain (via augmentation), enabling the model to be resilient to common LGE appearance variations. This approach is related to domain randomization [22], but is embedded within a few-shot adaptation framework. Our evaluation protocol tests robustness under deliberate and controlled distribution shifts, including an unseen LGE MRI dataset, allowing us to isolate the effect of distributional changes in line with established domain generalization practices [20].

In this paper, we propose a second-order MAML framework for K-shot 3D LA wall segmentation in LGE MRI, with (i) a multi-structure meta-training scheme that leverages abundant LA cavity and right atrial (RA) cavity annotations to learn features transferable to the thin LA wall; (ii) a controlled domain-shift protocol (simulated resolution loss, bias field, intensity, and noise/blur perturbations) with at least one unseen domain held out for meta-testing, plus evaluation on a private external LGE dataset, to rigorously assess robustness; (iii) an optimization and evaluation focus on thin structures, incorporating a composite loss (Dice, cross-entropy, and boundary losses) for thin-wall segmentation and emphasizing surface-based metrics to better capture clinically relevant boundary accuracy.

II. METHODS

A. Meta-learning formulation

We propose a gradient-based, meta-learning framework based on MAML that learns a parameter initialization, enabling rapid adaptation to 3D LGE-MRI LA wall segmentation using only K labeled volumes. The full pipeline is depicted in Fig. 1. In meta-training stage (a), the model optimizes its initial parameters for given tasks. Then, the model uses the generalized parameters and fine-tunes them for the new task, meta-testing stage (b). In testing stage, the model is evaluated on an unseen subset but belongs to the same testing task using the fine-tuned parameters. The approach is to meta-train on a family of related segmentation tasks, so the model can learn the atrial representations that transfer to the clinically challenging LA wall under both label scarcity and domain shift.

Let $\mathcal{D} = \{\mathcal{D}_{LA}, \mathcal{D}_{RA}, \mathcal{D}_{ext}\}$ denote our data sources of 3D LGE MRI volumes $x \in \mathbb{R}^{H \times W \times Z}$. \mathcal{D}_{LA} is the 2018 LA

Segmentation Challenge dataset with LA wall and LA cavity annotations (LA2018) [7]. \mathcal{D}_{RA} the RA segmentation dataset (RAS) with RA cavity annotations only [2]. \mathcal{D}_{ext} is a local cohort with LA wall annotations that is reserved exclusively for evaluation and never used in meta-training or meta-validation. We define a task as $\tau = (s, d)$, where s is the target structure (segmentation class) and d is the imaging domain (data distribution). In this work, $s \in \{LA_{wall}, LA_{cavity}, RA_{cavity}\}$. These targets are anatomically related yet differ substantially in segmentation difficulty: the cavities are larger and typically higher-contrast, while the LA wall is a thin, low-contrast structure. The domain, d , specifies whether images belong to the original (clean) LGE MRI distribution or to the synthetically shifted domain conditions, as defined below. By meta-training across both structures and domains, the model is encouraged to learn features that remain useful when annotations are scarce and the test distribution differs from the training distribution.

Each task, $\tau = (s, d)$, is a binary segmentation problem for structure s from images belonging to domain d . We sample a support set and query set at the subject level: $S_\tau = \{(x_i^d, y_i^s)\}_{i=1}^{K_\tau}$, $Q_\tau = \{(x_j^d, y_j^s)\}_{j=1}^{M_\tau}$, with S_τ and Q_τ containing disjoint subjects. Here, K_τ is small (e.g. 5) to simulate a K-shot scenario, and M_τ is the number of query cases used to evaluate adaptation. This support/query split follows standard episodic training for few-shot segmentation and explicitly mirrors a within-episode train/validation scenario used to compute the meta-loss [13], [14], [16].

For LA-wall tasks, we set $K_\tau = K$ with $K \in \{5, 10, 20\}$, such that the adaptation may rely on as few as a five labeled LA wall volumes. For auxiliary cavity tasks (LA-cavity, RA-cavity), we also enforce a small-support regime and cap the support size using $K_\tau = \min(K, K_{max})$, even when more cavity labels are available. This prevents the meta-objective from being dominated by large, easy support sets from auxiliary tasks and keeps the meta-gradient aligned with the intended few-shot adaptation setting. Meta-training then samples $\tau \sim p(\tau)$ over feasible (s, d) pairs, with $p(\tau)$ approximately uniform over s and over the selected training domains d (with a slight oversampling of LA-wall tasks to avoid over-bias toward the more straightforward cavity segmentation tasks). In practice, we maintain a balanced mix of tasks and increase the sampling frequency of LA-wall tasks, despite fewer available images, in order to reduce bias toward cavity segmentation. Each episode optimizes query-set error after adapting on the support set.

B. MAML Optimization for Segmentation

We train the model using the MAML algorithm [16]. This algorithm optimizes the initialization such that the model can adapt quickly to new tasks. Each meta-training iteration samples a meta-batch $\mathcal{B} = \{\tau_i\}_{i=1}^N$, with $\tau_i \sim p(\tau)$. We partition the model parameters into the adaptable subset θ (head and last decoder block) and the representation subset ϕ (encoder and early layers). For each task τ_i , we start from the current initialization θ and perform one inner-loop adaptation on its support set. With one inner update step:

$$\theta'_i = \theta - \alpha \nabla_\theta \mathcal{L}_{\tau_i}(S_{\tau_i}; \theta, \phi), \quad (1)$$

where $\mathcal{L}_{\tau_i}(\cdot)$ is the segmentation loss computed on S_{τ_i} and α is the inner-loop learning rate. In our implementation, this gradient step is applied only to the inner-loop-adapted subset (head and last decoder block), while the remaining parameters ϕ are held fixed during the inner step (ANIL-style inner-loop

adaptation [23]). Those fixed parameters (encoder and early layers) correspond to ϕ and are updated only by the outer-loop gradient based on query performance; only the inner-loop fine-tuning keeps these parameters unchanged. This preserves

stability in low-data updates while still meta-learning those parameters over many episodes. After this task-specific adaptation, the model is evaluated on the query set Q_{τ_i} .

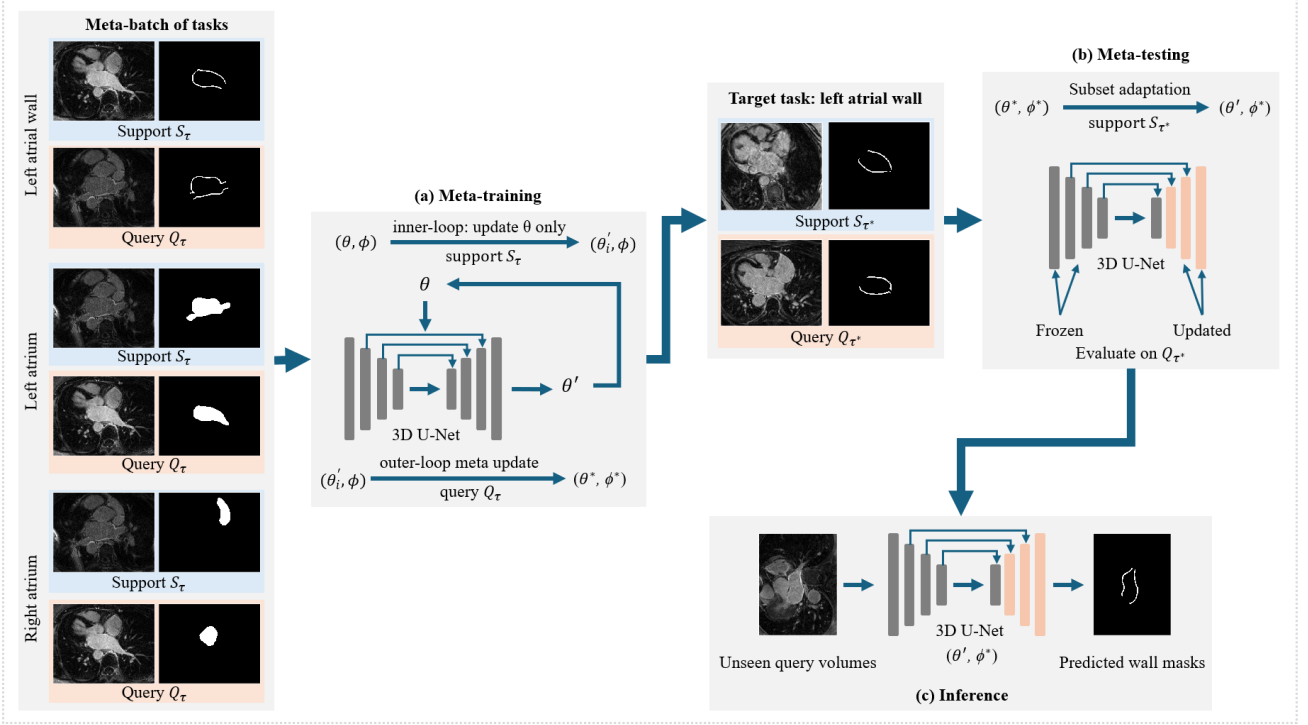


Fig. 1. Meta-learning pipeline for left atrium segmentation.

The outer loop then updates the initialization θ and the representation parameters ϕ to improve post-adaptation performance across all tasks in the batch:

$$\mathcal{L}_{\text{meta}}(\theta, \phi) = \sum_{i=1}^N \mathcal{L}_{\tau_i}(Q_{\tau_i}; \theta'_i, \phi), \quad (2)$$

$$(\theta, \phi) \leftarrow (\theta, \phi) - \beta \nabla_{(\theta, \phi)} \mathcal{L}_{\text{meta}}(\theta, \phi), \quad (3)$$

with meta learning rate β .

Second-order MAML is memory-intensive in 3D because it backpropagates through the inner-loop update. Following prior 3D MAML segmentation implementations [13], [14], we make training tractable in terms of GPU memory and runtime via: (i) patch-based learning (cropped sub-volumes), (ii) small inner-step count ($n=1$), (iii) gradient checkpointing, and (iv) mixed precision. At meta-test time (adaptation), we initialize the model with the meta-learned parameters (θ^*, ϕ^*) and fine-tune it on the LA wall target task in the target domain using K support volumes, producing adapted parameters $\theta'_{\text{LA-wall}}$, where ϕ remains fixed as $\phi = \phi^*$ under our subset-adaptation setting. We then apply the adapted model to segment query/test images from the same target domain. The methodological claim is that (θ^*, ϕ^*) , learned through episodic meta-training over tasks $\tau = (s, d)$, provides a stronger starting point than generic initialization or unrelated pre-training for LA wall delineation under limited labels and distribution shift. The inner and test-time adaptation learning rates are selected by episodic meta-validation (log-scale grid search). We prioritize second-order MAML over first-order approximations like Reptile to maximize adaptation fidelity,

given the importance of precise boundary optimization in our application, at the cost of higher computation [16], [24].

C. Network Architecture

We adopt a 3D residual U-Net segmentation model, configured following the established nnU-Net framework for biomedical imaging [25], [26], and adapted to our meta-learning setting. The network extracts features with $f_{\phi}(x)$ and produces a foreground probability map through a sigmoid head: $\hat{y} = \sigma(g_{\theta}(f_{\phi}(x)))$, $\hat{y} \in [0,1]^{H \times W \times Z}$, where $g_{\theta}(\cdot)$ is the output layer and $\sigma(\cdot)$ is the sigmoid. Because each task is binary (target structure vs. background), we use a single shared output head across all tasks. This avoids a multi-class formulation under partial annotation (e.g., RA-only) and keeps the model compact, while requiring the shared initialization to encode features that transfer across atrial structures after a few-shot update.

To improve stability under extremely small support sets and to reduce overfitting risk in the 3D implementation, we adapt only a subset of parameters during the inner loop: the segmentation head g_{θ} and the last decoder block of the U-Net. Earlier encoder/decoder layers (parameterized by ϕ) remain fixed during the inner update. This design preserves fast task-specific calibration while keeping adaptation well-conditioned in the low-data regime. To keep second-order meta-updates feasible, we use patch-based training on cropped 3D sub-volumes (e.g., 256^3 voxels) rather than full volumes, consistent with common practice for 3D U-Net training [2]. We use instance normalization to reduce sensitivity to intensity variation across domains. The network dropout rate

was set to 0.1, with a batch size of 1. Model parameters were optimized using the Adam optimizer, with a learning rate $\alpha = 1 \times 10^{-4}$, $\beta = 1 \times 10^{-6}$, and a weight decay of 1×10^{-5} . These hyperparameters were selected in accordance with best practices reported in the literature and further tuned empirically in our experiments [13].

D. Loss Functions

Each task-specific segmentation loss \mathcal{L}_τ combines region-based overlap terms with a boundary-aware term designed for extreme class imbalance and thin anatomy. For a predicted probability map \hat{y} and ground-truth binary mask y , we define:

$$\mathcal{L}_\tau = \lambda_D \mathcal{L}_{Dice} + \lambda_{CE} \mathcal{L}_{CE} + \lambda_B \mathcal{L}_{boundary}, \quad (4)$$

Here $\lambda_D, \lambda_{CE}, \lambda_B$ weight the Dice, cross-entropy (CE), and boundary loss components. We use soft Dice loss to mitigate class imbalance [27]:

$$\mathcal{L}_{Dice} = 1 - \frac{2 \sum_i \hat{y}_i y_i + \epsilon}{\sum_i \hat{y}_i + \sum_i y_i + \epsilon'}, \quad (5)$$

where $\hat{y}_i \in [0,1]$, $y_i \in \{0,1\}$, and ϵ is a smoothing constant (e.g., 10^{-6}), and i indexes voxels ($i = 1, \dots, V$). We include binary cross-entropy for per-voxel supervision and better calibration:

$$\mathcal{L}_{CE} = -\frac{1}{V} \sum_i [y_i \log(\hat{y}_i) + (1 - y_i) \log(1 - \hat{y}_i)], \quad (6)$$

where V is the number of voxels. Unlike Dice, CE provides stable gradients even when overlap is initially poor. In practice, Dice+CE often improves convergence and accuracy compared to Dice alone (this combined loss is used in many state-of-the-art segmentation frameworks) [27], [28]. To refine thin boundaries, we incorporate the boundary loss [27]. Let $\phi_Y(i)$ be the signed distance (level-set) map of the ground truth boundary (negative foreground, positive outside). The boundary loss is:

$$\mathcal{L}_{boundary} = \frac{1}{V} \sum_i \hat{y}_i \phi_Y(i), \quad (7)$$

which encourages probability mass to concentrate on the correct side of the ground-truth boundary and improves surface alignment for thin structures. Loss weights $\lambda_D, \lambda_{CE}, \lambda_B$ are selected by episodic meta-validation. We apply the same composite loss during few-shot adaptation at meta-test time for consistency.

E. Datasets and Controlled Domain Shift Protocol

We use the public LA2018 dataset [7] (154 LGE MRI volumes with LA cavity and wall annotations). Let \mathcal{D}_{LA}^{train} and \mathcal{D}_{LA}^{test} denote the 124/30 subject-level split of LA2018, 124 cases for meta-training/meta-validation and 30 cases for meta-testing. For each domain $d_k \in \{d_0, \dots, d_4\}$, we construct domain-specific variants $\mathcal{D}_{LA}^{train}(d_k)$ and $\mathcal{D}_{LA}^{test}(d_k)$ by applying T_{d_k} to images while keeping masks unchanged. Meta-training draws episodes only from $\mathcal{D}_{LA}^{train}(d_k)$ with $d_k \in \{d_0, d_1, d_2, d_3\}$, while evaluation uses $\mathcal{D}_{LA}^{test}(d_0)$ (clean) and $\mathcal{D}_{LA}^{test}(d_4)$ (unseen shift).

From the subset of 124 cases, we hold out a subset (e.g., 20 cases) for episodic meta-validation to tune hyperparameters and early stopping (not used in meta-training episodes). For auxiliary RA-cavity supervision, we use the RAS dataset [2] (50 LGE MRI volumes with RA cavity annotations only). These are used only for RA cavity tasks during meta-training and are split into train/validation partitions analogously.

A distinct, local cohort of 42 LGE MRI scans acquired from patients with persistent atrial fibrillation with LA wall and LA cavity ground truth is reserved entirely for evaluation under a genuine unseen distribution and is not used for meta-training, meta-validation, or hyperparameter selection.

All volumes are cropped and resampled to a consistent orientation and voxel size (e.g., 0.625 mm isotropic for internal processing), then intensity-normalized per volume by clipping extreme values and scaling to zero-mean unit-variance. Synthetic domain transforms are generated on-the-fly during meta-training to avoid reducing the effective dataset size while increasing appearance diversity. We perform subject-level splits into meta-train, meta-validation, and meta-test partitions to prevent patient leakage. For each meta-test episode, we sample an LA-wall task on held-out subjects and construct a K -shot support set and a disjoint query set from the same held-out partition.

Real-world LGE MRI signal intensity varies across scanners and acquisition settings, causing domain shifts that degrade segmentation performance. To evaluate and improve robustness, we introduce a controlled domain shift protocol with synthetic transformations. We define: $\mathcal{D}_{shift} = \{d_0, d_1, \dots, d_4\}$, where d_0 is the clean domain and d_1-d_4 are altered domains that mimic common LGE variations. Each domain corresponds to a transformation $T_d(x)$ applied to images, while the segmentation masks remain unchanged. The clean domain d_0 uses standard preprocessing and intensity normalization. The resolution-shift domain d_1 downsamples images in-plane (e.g., $2 \times$) then upsamples back, inducing blur and partial-volume effects. The bias-field domain d_2 multiplies images by a smooth low-frequency field to emulate intensity inhomogeneity [21]. The contrast-variation domain d_3 applies gamma/histogram scaling to simulate global intensity/contrast differences. Finally, the noise-and-blur domain d_4 introduces additive noise and mild blur to simulate degraded image quality.

We train on $\mathcal{D}_{train} \subset \mathcal{D}_{shift}$ and hold out at least one domain as unseen: $\mathcal{D}_{test} = \mathcal{D}_{shift} \setminus \mathcal{D}_{train}$ [19], [20]. In our primary protocol, we exclude d_4 from meta-training and reserve it for meta-testing as an unseen synthetic shift.

During meta-training, transformations are sampled on-the-fly within \mathcal{D}_{train} to increase diversity. To prevent leakage, we first perform a subject-level split once on the underlying clean data (meta-train/meta-val/meta-test), and then generate each domain d_k by applying T_{d_k} only within the corresponding split. Thus, each subject (and all of its domain-transformed variants) belongs to exactly one partition. During evaluation, domain transforms are applied deterministically for reproducible reporting.

During evaluation, domain transforms are applied deterministically for reproducible reporting. We further evaluate on the local cohort of 42 LGE MRI scans with LA wall annotations as an additional unseen test domain d_{ext} . This dataset is never used in meta-training and is reserved for evaluation under genuine distribution shift.

F. Few-shot evaluation protocol

We evaluate few-shot performance for $K \in \{5, 10, 20\}$ using an episodic meta-test protocol that mimics deployment. For each K , we sample multiple meta-test episodes; each episode adapts on K labeled support volumes and is evaluated on M disjoint query volumes drawn from the same meta-test pool

(and, for domain-shift experiments, from d_4). Within each meta-test episode, “meta-testing” refers to K -shot adaptation on the support set, and “final testing/inference” refers to evaluating the adapted model on the disjoint query set.

Our primary target is LA wall segmentation, and we consider three scenarios: (a) Clean (in-domain) K -shot adaptation and evaluation on the held-out 30 LA wall cases; (b) Unseen synthetic domain K -shot adaptation and evaluation within the unseen domain d_4 , using support/query volumes drawn from $\mathcal{D}_{LA}^{test}(d_4)$; and (c) External dataset K -shot adaptation on K labeled cases from a private external LGE cohort (d_{ext}) and evaluation on the remaining external cases. Performance is averaged across multiple random episodes for each scenario.

We evaluated and compared three models. The first model, K -shot supervised fine-tuning (FT) uses the same 3D U-Net, pre-trained on a source set (e.g., cavity-labeled data) and then fine-tuned per episode using only the K LA wall support volumes; the model is optimized for a fixed adaptation budget and evaluated on disjoint query volumes from the same target pool, serving as a practical few-shot baseline without a meta-learned initialization. The proposed MAML model performs episodic meta-training across structures and training domains, followed by K -shot adaptation to the LA-wall task. Finally, the full supervision model (Full-sup) trains the same 3D U-Net using all available LA-wall labels in the training partition and is reported only as a supervised upper bound, since it is not comparable in annotation cost to few-shot methods. All methods share the same backbone, preprocessing, and loss definition, with adaptation hyperparameters selected via episodic meta-validation.

G. Metrics

We report Dice coefficient (DSC) as the primary overlap metric. We also report HD95 (95th Percentile Hausdorff Distance in mm) to capture worst-case boundary error and NSD (normalized surface dice) as a surface-based measure. For NSD, we use a tolerance of 2 mm, reflecting the approximate mean LA wall thickness in humans. Surface metrics are emphasized because thin-wall segmentation is boundary-dominated: small surface shifts can create clinically meaningful thickness distortions while only modestly changing overlap [29]. All metrics are computed in 3D per case and averaged over the evaluation set. We report the mean and standard deviation of performance metrics across episodes to reduce sensitivity to any particular support selection.

III. RESULTS AND DISCUSSION

Table I reports the K -shot performance on the clean test domain d_0 using unseen subjects. Support and query are drawn from the held-out d_0 pool with disjoint cases per episode. Across $K \in \{5, 10, 20\}$, the proposed MAML achieves the best mean DSC and NSD, with consistently lower variability than the non-meta baseline (FT). At $K=5$, MAML improves DSC from 0.590 ± 0.070 (FT) to 0.645 ± 0.045 and NSD from 0.480 ± 0.085 to 0.535 ± 0.060 , suggesting better accuracy and surface alignment. HD95 (mm) shows a consistent reduction from the FT model, decreasing from 6.60 ± 1.35 (FT) to 5.70 ± 1.05 (MAML) at $K=5$, which suggests fewer extreme boundary outliers and improved worst-case surface errors. Similar trends hold at $K=10$ and $K=20$, where MAML maintains a consistent advantage over FT in both

overlap and surface-based accuracy. These gains are most meaningful in the low-shot regime, where wall-only training is highly sensitive to initialization and boundary ambiguity. The LA wall is thin and low-contrast, so small changes in initialization can lead to large differences in the final boundary. MAML directly optimizes the initialization for rapid post-update improvement, which is aligned with the intended K -shot deployment scenario and the original motivation of gradient-based meta-learning [16]. In practice, this optimization objective manifests as: (i) improved mean performance at small K , and (ii) reduced variance across episodes, because the meta-learned initialization is less brittle to which specific K cases are selected as support. Relative to the Full-sup (0.706 ± 0.042 DSC), the meta-learned (MAML) results at $K=20$ (0.692 ± 0.032) approach the fully supervised ceiling. The same trend is reflected in boundary accuracy: MAML approaches the fully supervised NSD and HD95 ($0.781, 4.02$ mm), reaching $0.765, 4.35$ mm at $K=20$.

Table II summarizes MAML’s K -shot LA wall adaptation under two unseen shifts: the held-out synthetic domain d_4 and the local cohort d_{ext} . Relative to clean d_0 performance (Table I) both shifts introduce the expected degradation, with the effect more apparent in surface accuracy than overlap. On d_4 , MAML achieves 0.59 DSC, 0.66 NSD, and 5.99 mm HD95 at $K=5$, improving steadily to $0.64/0.71/5.05$ at $K=10$ and $0.68/0.73/4.83$ at $K=20$, indicating that additional support labels consistently reduce worst-case boundary errors under the synthetic perturbation. Performance on the local cohort appears reduced overall, with $0.57/0.63/6.01$ at $K=5$ and $0.63/0.69/5.55$ at $K=10$, and it approaches the synthetic-shift regime at $K=20$ (0.67 DSC, 0.71 NSD, 4.95 mm HD95). Notably, the largest gap between d_4 and d_{ext} appears in HD95 at $K=10$ (5.05 vs. 5.55 mm), which is consistent with thin-wall delineation being especially sensitive to real scanner/protocol differences that manifest as localized boundary outliers even when mean overlap remains comparable.

Fig.2 shows representative 5-shot LA-wall segmentations on unseen d_0 cases and the local cohort d_{ext} . Compared with FT, MAML yields more continuous wall boundaries with fewer fragmented predictions, particularly in low-contrast regions. This visual pattern is consistent with improved surface alignment and reduced HD95, suggesting fewer episodes dominated by large boundary outliers in the low-shot setting.

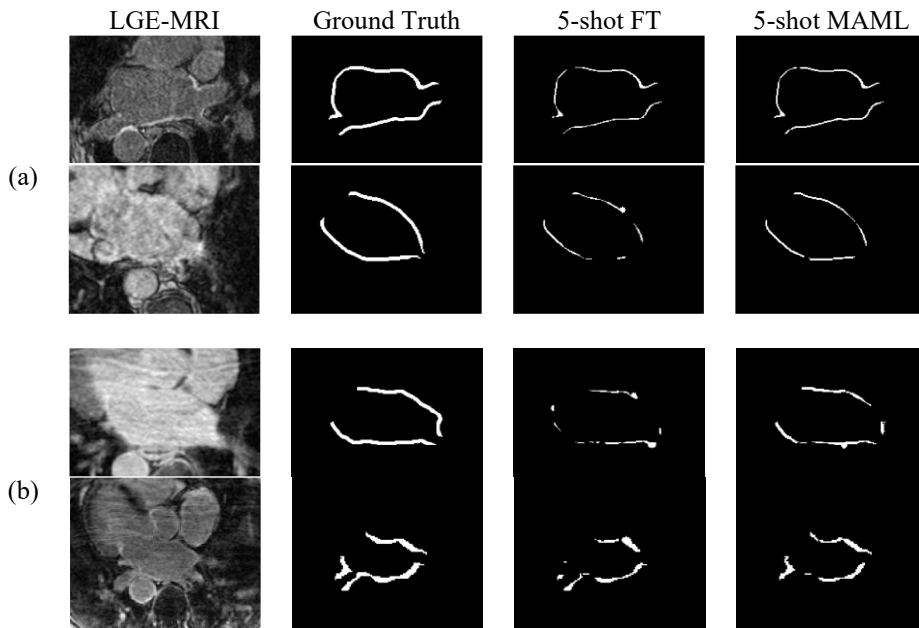
This behavior supports the claim that the meta-learned initialization yields smaller degradation under unseen shifts than direct K -shot training, because meta-training exposes the learner to a distribution of tasks (s, d) and forces the initialization to remain usable after a small number of adaptation steps. By incorporating auxiliary cavity tasks, we bias the representation toward atrial anatomy and stable shape cues, while reserving wall labels for task-specific adaptation. In other words, cavity tasks provide strong anatomical context (e.g., global atrial geometry), while MAML ensures that the resulting features remain adaptable to the wall with limited labels. This design is aligned with meta-learning practice in medical segmentation [13], [14]. Across Tables I–II, MAML’s improvements come with more consistent episode-level behavior, most noticeably at low K .

TABLE I. K-SHOT ADAPTATION RESULTS ON UNSEEN CLEAN TEST SET.

Method	K=5			K=10			K=20		
	DSC \uparrow	NSD \uparrow	HD95 \downarrow	DSC \uparrow	NSD \uparrow	HD95 \downarrow	DSC \uparrow	NSD \uparrow	HD95 \downarrow
FT	0.52 ± 0.06	0.55 ± 0.07	7.60 ± 1.35	0.53 ± 0.05	0.57 ± 0.06	6.65 ± 1.10	0.55 ± 0.04	0.58 ± 0.06	6.05 ± 0.98
MAML	0.64 ± 0.05	0.72 ± 0.06	5.70 ± 1.05	0.670 ± 0.04	0.75 ± 0.05	4.85 ± 0.92	0.69 ± 0.03	0.765 ± 0.05	4.35 ± 0.86
Full-sup	0.71 ± 0.04	0.78 ± 0.04	4.02 ± 0.88	0.71 ± 0.04	0.78 ± 0.04	4.02 ± 0.88	0.71 ± 0.04	0.78 ± 0.04	4.02 ± 0.88

TABLE II. K-SHOT ADAPTATION RESULTS ON d_0/d_{ext} (UNSEEN SHIFT) USING K-SHOT ADAPTATION

d	K=5			K=10			K=20		
	DSC \uparrow	NSD \uparrow	HD95 \downarrow	DSC \uparrow	NSD \uparrow	HD95 \downarrow	DSC \uparrow	NSD \uparrow	HD95 \downarrow
d_4	0.59 ± 0.05	0.66 ± 0.07	5.99 ± 1.35	0.64 ± 0.04	0.71 ± 0.06	5.05 ± 1.15	0.68 ± 0.03	0.73 ± 0.05	4.83 ± 1.02
d_{ext}	0.57 ± 0.05	0.63 ± 0.08	6.01 ± 1.55	0.63 ± 0.05	0.69 ± 0.07	5.55 ± 1.25	0.67 ± 0.04	0.71 ± 0.06	4.95 ± 1.10

Fig. 2. Axial mid-slice comparison of LA wall segmentation with $K = 5$. Cases are drawn from (a) unseen domain d_0 subjects and (b) the local cohort d_{ext} .

On the clean domain d_0 (Table I), MAML exhibits a smaller episode-to-episode spread than FT, especially at $K=5$, suggesting reduced sensitivity to which subjects are selected for the support set.

This is impactful in a deployment-style K -shot protocol, where performance can fluctuate with support composition and with boundary ambiguity in low-contrast regions. We do not attribute this stability to a single mechanism; instead, it is in line with the way the method is trained and applied, i.e., MAML optimizes for post-update performance across episodes, and we further regularize low-shot adaptation by restricting inner-loop updates to the head and last decoder block. The same reliability signal is reflected in surface error: the tighter HD95 variability on d_0 , together with the unseen-shift performance in Table 2, indicates fewer episodes with large boundary outliers, which is particularly important for thin LA-wall delineation where localized failures can dominate worst-case surface metrics even when overlap changes modestly. The controlled domain shift protocol, while transparent and reproducible, remains a synthetic approximation of real multi-site heterogeneity (e.g., coil differences, vendor-specific reconstruction, gating variability, and population/pathology shifts); therefore, our generalization claims are explicitly bounded to the defined shift family and the held-out evaluation partitions, with additional real-world evidence provided by the local cohort d_{ext} . Our design

choices reflect practical constraints of 3D few-shot meta-learning: subset adaptation (head + last decoder block) improves stability and reduces low-shot overfitting but can limit adaptation capacity compared to full-network fine-tuning when more labels are available (e.g., $K = 20$), while full second-order MAML improves meta-optimization fidelity yet remains computationally demanding despite checkpointing and mixed precision [13], [14], [16]. Future work should therefore prioritize broader external validation across multiple institutions and scanners, and adopt more rigorous robustness assessments (e.g., leave-one-domain-out across $d_1 \dots d_4$) to quantify sensitivity to unseen shifts under a standardized protocol. Finally, because LA wall delineation is boundary-dominated and limited by partial-volume effects, future work could incorporate thin-structure-tailored objectives or representations to further improve few-shot adaptation, e.g., learning distance transforms/signed distance fields, centerline/skeleton constraints, thickness-consistency regularization, or surface-based losses that directly optimize NSD/HD95.

IV. CONCLUSION

Quantifying left atrial wall remodeling is clinically important for characterizing atrial cardiomyopathy and informing ablation planning in atrial fibrillation, yet accurate wall delineation in LGE MRI remains difficult due to the

wall's thinness, low contrast, and strong sensitivity to acquisition variability. In this work, we presented a second-order MAML framework for label-efficient 3D LA wall segmentation, meta-trained across related atrial structures (LA/RA cavities and LA wall) and multiple training domains to learn an initialization that supports rapid K-shot adaptation. Across clean and unseen-shift evaluations, including a held-out synthetic shift and a distinct local cohort, the meta-learned initialization consistently improved overlap and surface accuracy in the low-shot regime and showed more reliable episode-level behavior, with fewer large boundary outliers. These findings suggest that meta-learning can reduce the dependence on large, center-specific LA-wall datasets and enable practical adaptation to new clinical environments using only a handful of annotated cases. This capability has the potential to lower barriers for deploying automated atrial analysis pipelines in multi-center studies and, ultimately, routine clinical workflows.

ACKNOWLEDGMENT

This research was enabled in part by the Natural Sciences and Engineering Research Council of Canada (NSERC) Discovery Grant, and by computational resources provided by the Digital Research Alliance of Canada (<https://alliancecan.ca>).

REFERENCES

- [1] Y. Wu, Z. Tang, B. Li, D. Firmin, and G. Yang, "Recent Advances in Fibrosis and Scar Segmentation From Cardiac MRI: A State-of-the-Art Review and Future Perspectives," *Front. Physiol.*, vol. 12, p. 709230, Aug. 2021, doi: 10.3389/FPHYS.2021.709230.
- [2] J. Zhu et al., "RAS Dataset: A 3D Cardiac LGE-MRI Dataset for Segmentation of Right Atrial Cavity," *Sci. Data*, vol. 11, no. 1, p. 401, Dec. 2024, doi: 10.1038/S41597-024-03253-9.
- [3] A. S. Ismail, Y. Baghdady, M. A. Salem, and A. A. Wahab, "The use of MRI in quantification of the atrial fibrosis in patients with rheumatic mitral disease," *Egyptian Journal of Radiology and Nuclear Medicine*, vol. 51, no. 1, Dec. 2020, doi: 10.1186/s43055-020-00322-y.
- [4] J. Ma, Q. Chen, and S. Ma, "Left atrial fibrosis in atrial fibrillation: Mechanisms, clinical evaluation and management," Mar. 01, 2021, John Wiley and Sons Inc. doi: 10.1111/jcmm.16350.
- [5] L. Li, V. A. Zimmer, J. A. Schnabel, and X. Zhuang, "Medical Image Analysis on Left Atrial LGE MRI for Atrial Fibrillation Studies: A Review," *Med. Image Anal.*, vol. 77, p. 102360, Apr. 2022, doi: 10.1016/J.MEDIA.2022.102360.
- [6] H. Lin et al., "Usformer: A small network for left atrium segmentation of 3D LGE MRI," *Heliyon*, vol. 10, no. 7, Apr. 2024, doi: 10.1016/j.heliyon.2024.e28539.
- [7] Z. Xiong et al., "A global benchmark of algorithms for segmenting the left atrium from late gadolinium-enhanced cardiac magnetic resonance imaging," *Med. Image Anal.*, vol. 67, Jan. 2021, doi: 10.1016/j.media.2020.101832.
- [8] G. Yang et al., "Simultaneous left atrium anatomy and scar segmentations via deep learning in multiview information with attention," *Future Generation Computer Systems*, vol. 107, pp. 215–228, Jun. 2020, doi: 10.1016/j.future.2020.02.005.
- [9] L. Li, V. A. Zimmer, J. A. Schnabel, and X. Zhuang, "AtrialJSQnet: A New framework for joint segmentation and quantification of left atrium and scars incorporating spatial and shape information," *Med. Image Anal.*, vol. 76, Feb. 2022, doi: 10.1016/j.media.2021.102303.
- [10] C. Thesing, A. Bueno-Orovio, and A. Banerjee, "Evaluating Convolution, Attention, and Mamba Based U-Net Models for Multi-class Bi-Atrial Segmentation from LGE-MRI," in *Lecture Notes in Computer Science*, Springer Science and Business Media Deutschland GmbH, 2025, pp. 214–225. doi: 10.1007/978-3-031-87756-8_22.
- [11] E. Almar-Munoz et al., "Multi-loss 3D Segmentation for Enhanced Bi-atrial Segmentation," in *Lecture Notes in Computer Science*, Springer Science and Business Media Deutschland GmbH, 2025, pp. 236–244. doi: 10.1007/978-3-031-87756-8_24.
- [12] A. Zolotarev, K. Johnson, A. Khan, G. Slabaugh, and C. Roney, "An Ensemble of 3D Residual Encoder UNet Models for Solving Multi-class Bi-atrial Segmentation Challenge," in *Lecture Notes in Computer Science*, Springer Science and Business Media Deutschland GmbH, 2025, pp. 209–213. doi: 10.1007/978-3-031-87756-8_21.
- [13] A. M. Alsaleh, E. Albalawi, A. Algoasibi, S. S. Albakheet, and S. B. Khan, "Few-Shot Learning for Medical Image Segmentation Using 3D U-Net and Model-Agnostic Meta-Learning (MAML)," *Diagnostics (Basel)*, vol. 14, no. 12, Jun. 2024, doi: 10.3390/DIAGNOSTICS14121213.
- [14] R. Khadka et al., "Meta-learning with implicit gradients in a few-shot setting for medical image segmentation," *Comput. Biol. Med.*, vol. 143, p. 105227, Apr. 2022, doi: 10.1016/J.COMPBIOMED.2022.105227.
- [15] S. Tang et al., "Few-shot Medical Image Segmentation with High-Fidelity Prototypes," *Med. Image Anal.*, vol. 100, p. 103412, Feb. 2025, doi: 10.1016/J.MEDIA.2024.103412.
- [16] C. Finn, P. Abbeel, and S. Levine, "Model-Agnostic Meta-Learning for Fast Adaptation of Deep Networks," Jul. 17, 2017, PMLR. Accessed: Jan. 13, 2026. [Online]. Available: <https://proceedings.mlr.press/v70/finn17a.html>
- [17] P. H. T. Gama, H. Oliveira, and J. A. Dos Santos, "Learning to Segment Medical Images from Few-Shot Sparse Labels," *SIBGRAPI Conference on Graphics, Patterns and Images*, pp. 89–96, 2021, doi: 10.1109/SIBGRAPI54419.2021.00021.
- [18] J. Chen et al., "Adaptive dynamic inference for few-shot left atrium segmentation," *Med. Image Anal.*, vol. 98, Dec. 2024, doi: 10.1016/j.media.2024.103321.
- [19] H. Guan and M. Liu, "Domain Adaptation for Medical Image Analysis: A Survey," *IEEE Trans. Biomed. Eng.*, vol. 69, no. 3, p. 1173, Mar. 2022, doi: 10.1109/TBME.2021.3117407.
- [20] J. S. Yoon, K. Oh, Y. Shin, M. A. Mazurowski, and H. Il Suk, "Domain Generalization for Medical Image Analysis: A Review," *Proceedings of the IEEE*, vol. 112, no. 10, pp. 1583–1609, 2024, doi: 10.1109/JPROC.2024.3507831.
- [21] Z. Niu, S. Ouyang, S. Xie, Y. Chen, and L. Lin, "A Survey on Domain Generalization for Medical Image Analysis," Feb. 2024, Accessed: Jan. 13, 2026. [Online]. Available: <https://arxiv.org/pdf/2402.05035v1>
- [22] Z. Ye, K. Wang, W. Lv, Q. Feng, and L. Lu, "FSDA-DG: Improving Cross-Domain Generalizability of Medical Image Segmentation with Few Source Domain Annotations," *Med. Image Anal.*, vol. 105, p. 103704, Oct. 2025, doi: 10.1016/J.MEDIA.2025.103704.
- [23] A. Raghu, M. Raghu, S. Bengio, and O. Vinyals, "Rapid Learning or Feature Reuse? Towards Understanding the Effectiveness of MAML," 8th International Conference on Learning Representations, ICLR 2020, Sep. 2019, Accessed: Jan. 22, 2026. [Online]. Available: <https://arxiv.org/pdf/1909.09157>
- [24] A. Nichol, J. Achiam, and J. Schulman, "On First-Order Meta-Learning Algorithms," *arXiv.org*, 2018.
- [25] O. Ronneberger, P. Fischer, and T. Brox, "U-Net: Convolutional Networks for Biomedical Image Segmentation," *Lecture Notes in Computer Science (including subseries Lecture Notes in Artificial Intelligence and Lecture Notes in Bioinformatics)*, vol. 9351, pp. 234–241, 2015, doi: 10.1007/978-3-319-24574-4_28.
- [26] Ö. Çiçek, A. Abdulkadir, S. S. Lienkamp, T. Brox, and O. Ronneberger, "3D U-net: Learning dense volumetric segmentation from sparse annotation," *Lecture Notes in Computer Science (including subseries Lecture Notes in Artificial Intelligence and Lecture Notes in Bioinformatics)*, vol. 9901 LNCS, pp. 424–432, 2016, doi: 10.1007/978-3-319-46723-8_49/TABLES/3.
- [27] H. Kervadec, J. Bouchtiba, C. Desrosiers, E. Granger, J. Dolz, and I. Ben Ayed, "Boundary loss for highly unbalanced segmentation," *Med. Image Anal.*, vol. 67, Jan. 2021, doi: 10.1016/j.media.2020.101851.
- [28] F. Isensee, P. F. Jaeger, S. A. A. Kohl, J. Petersen, and K. H. Maier-Hein, "nnU-Net: A Self-Configuring Method for Deep Learning-Based Biomedical Image Segmentation," *Nature Methods* 2020 18:2, vol. 18, no. 2, pp. 203–211, Dec. 2020, doi: 10.1038/s41592-020-01008-z.
- [29] S. Nikolov et al., "Clinically Applicable Segmentation of Head and Neck Anatomy for Radiotherapy: Deep Learning Algorithm Development and Validation Study," *J. Med. Internet Res.*, vol. 23, no. 7, Jul. 2021, doi: 10.2196/26151